

# The ORCA-TWIN qCMOS Project

## I. Commissioning at Calar Alto Observatory

Martin M. Roth<sup>1, 2, 3, \*</sup>, Paško Roje<sup>1</sup>, Stella Vješnica<sup>1</sup>, Stefan Cikota<sup>5, 7</sup>, Alex J. Brown<sup>4</sup>, Mike Kretlow<sup>1, 6</sup>, Marco Azzaro<sup>5</sup>, Santiago Reinhart<sup>5</sup>, Jesús Aceituno<sup>5</sup>, and Thomas Kupfer<sup>4, 8</sup>

<sup>1</sup> Deutsches Zentrum für Astrophysik (DZA), Postplatz 1, 02826 Görlitz, Germany

<sup>2</sup> Leibniz-Institut für Astrophysik Potsdam (AIP), An der Sternwarte 16, 14482 Potsdam, Germany

<sup>3</sup> Institut für Physik und Astronomie, Universität Potsdam, Karl-Liebknecht-Str. 24/25, 14476 Potsdam, Germany

<sup>4</sup> Hamburger Sternwarte, University of Hamburg, Gojenbergsweg 112, 21029 Hamburg, Germany  
<sup>5</sup> Centro de Astrofísica da Universidade de Lisboa, Orléans 2690-426, Portugal

<sup>6</sup> Centro Astronómico Hispano en Andalucía, Observatorio de Calar Alto, Sierra de los Filabres, E-04550 Gérgal, Spain

<sup>7</sup> Instituto de Astrofísica de Andalucía (IAA-CSIC), Glorieta de la Astronomía, s/n, 18008 Granada, Spain.

<sup>7</sup> University of Zagreb, Faculty of Electrical Engineering and Computing, Department of Communication and Space Technologies, Unska 3, 10000 Zagreb, Croatia

<sup>8</sup> Department of Physics and Astronomy, Texas Tech University, Lubbock, TX 79409-1051, USA

Received : accepted

Received ; accepted

## ABSTRACT

**Aims.** We describe a pilot study to explore a new generation of fast and low noise CMOS image sensors for time domain astronomy, using two remote telescopes with a baseline of 1800 km.

**Methods.** Direct imaging with novel qCMOS image sensor technology that combines fast readout with low readout noise. Synchronized observations from two remote telescope sites will be used to explore new approaches for measuring solar system bodies, precision stellar photometry, and speckle imaging.

**Results.** A fast-track installation of an ORCA-Quest 2 camera at the Calar Alto Observatory (CAHA) 1.23m telescope has demonstrated the potential of the qCMOS technology for time domain astronomy.

**Conclusions.** qCMOS technology generally outperforms classical CCDs for high-cadence imaging on 1-m telescopes, although EMCCDs remain competitive, and in some cases slightly superior, for very short exposures and faint sources.

**Key words.** instrumentation: direct imaging – time domain astronomy: short period binaries – solar system objects: asteroids – near Earth objects

## 1. Introduction

From a historical perspective, charge coupled devices (CCD) have enabled from the 1980s a breakthrough for astronomy in the visible, with impact on almost all kinds of observing techniques, from direct imaging, over spectroscopy, to high precision polarimetry, whether in space, or at ground-based observatories. After three decades of development and constant improvement, the modern CCD must be considered a mature technology, and an almost ideal detector for scientific applications, providing high quantum efficiency (QE), low read noise, excellent linearity, and a large dynamic range (Roth 2023). The one drawback for time-domain astronomy, however, is its principle of operation: charge transfer means a slow readout process through the bottleneck of one (or a few) output nodes. For fast cadence observations, the deadtime for readout between exposures makes it prohibitive to use full frame CCDs for cadence shorter than 10 s.

As a variant of the classical CCD that overcomes this disadvantage, the Electron Multiplication CCD (EMCCD, also LLL-CCD for low light level CCD, or L3CCD) was introduced by [Jerram et al. \(2001\)](#) as a sensor where individual photoelectrons are amplified in a series of high voltage electrodes, resulting in ionization of secondary electrons and a cascade of charge with

an output node voltage that is much higher than the read noise, thus the ability to detect single photons. Therefore, EMCCDs have found use for astronomical applications with very short exposure times and high cadence. The properties of EMCCDs in comparison with CCDs are discussed in detail by [Smith et al. \(2004\)](#); [Mackay et al. \(2004\)](#); [Burke et al. \(2005\)](#). In summary, the EMCCD features sub-electron readout noise, high readout speed, and high quantum efficiency. Amongst the drawbacks, it exhibits multiplication noise, a low dynamic range, and an undesirable background from clock induced charge.

From the early 2000s, CMOS image sensors were beginning to enter the arena of scientific detectors, e.g., Janesick et al. (2002); Ay et al. (2002). A comprehensive summary of CMOS properties was presented in a series of conference papers by Janesick et al. (2006); Janesick et al. (2007, 2009, 2010). As opposed to the slow serial readout of the CCD, the architecture of this type of sensor (also alluded to as "active pixel sensor") provides a readout node in each pixel. Multiplex access to the individual pixel charges/voltages allows for fast readout of the entire sensor, and frame rates of order 100 fps, or even faster. Detectors that are, as opposed to consumer applications, optimized for scientific imaging, are often called sCMOS. The use of sCMOS sensors for space applications was discussed by Jerram & Stefanov (2020). A critical review of sCMOS sensors in com-

---

\* Corresponding author: mmroth@aip.de

parison to CCD for astronomy was presented by [Hodapp & Hall \(2006\)](#). At present, this type of detector is predominantly found in space application, e.g. remote sensing, but on the ground it is still mostly limited to amateur astronomy.

An interesting sCMOS sensor development from BAE Systems with high QE (70% at 600 nm), low read noise ( $1 \text{ e}^-$ ), and fast readout (100 fps) was presented by [Vu et al. \(2012\)](#). It has been further optimized and is now available as a  $4000 \times 2300$  pixel back-side illuminated device from Fairchild Imaging (the company was renamed in 2024 after acquisition by Hamamatsu). The astronomical image sensor community was made aware of an off-the-shelf camera system available from Hamamatsu, based on this chip, at the Scientific Detector Workshop 2022, which had a peculiar focus on quanta sensors that can detect single photons, such as skipper CCDs, or low-noise CMOS ([Amico et al. 2023](#)). Although two years later applications for speckle interferometry at the Sternberg 2.5m Telescope ([Strakhov et al. 2024](#)) and for the Visible Aperture-Masking Polarimetric Imager/Interferometer with extreme adaptive optics at the Subaru Telescope ([Lucas et al. 2024](#)) were reported to have made use of the Hamamatsu camera, that comes with the brand name ORCA-Quest<sup>1</sup>, not many other applications for astronomy are known to date.

The technology has found interest for Space applications ([Krynski et al. 2025b](#)), also with regard to another device, the GigaJot GJ01611, that used to be commercially available in the GigaJot QIS16 camera ([Ma et al. 2021](#)), which, however, has disappeared from the market. The back-illuminated sensor featured very low read-noise of  $0.19 \text{ e}^-$  in a format of  $4096 \times 4096$  pixels, however at the expense of tiny pixels with a pitch of  $1.1 \mu\text{m}$  ([Krynski et al. 2025a](#)).

Because of the relevance for future developments, the term qCMOS will be used in the following as a general definition for *very low read-noise, quanta CMOS sensors*, regardless of commercial branding.

The emerging German Center for Astrophysics (DZA) in Görlitz, Germany, that was founded as a legal entity in September 2025, with a mission to perform, firstly, fundamental research in astrophysics, secondly, technology development for astronomical instrumentation, and thirdly, big data analysis, discovered that the commercially available ORCA-Quest camera would motivate interesting science cases for time domain astronomy within the envisaged research portfolio, and possibly a fast track pilot study at 1m-class telescopes. Here we report on the implementation of this idea within the ORCA-TWIN project, and the first steps to realization.

The paper is organized as follows: Section 2 introduces the science case and concept, Sect. 3 discusses the advance of the qCMOS technology over classical image sensors, Sect. 4 numerical simulations of performance at the telescope, Sect. 5, commissioning of one of two cameras at Calar Alto, and Sect. 6 the results from the first observations. We close the paper with conclusions and an outlook in Sect. 7.

## 2. The ORCA-TWIN Concept

Motivated by an initial focus of the DZA research agenda on multi-messenger and time domain astronomy, also the vision to engage the regional semiconductor eco-system around Dresden for the development of novel image sensors, the procurement of

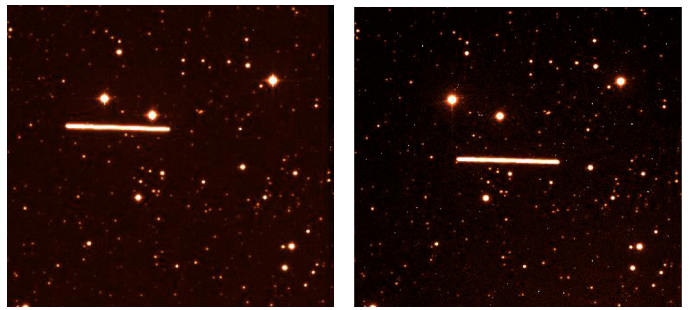


**Fig. 1.** Simultaneous observations of asteroid 4179 Toutatis, left: WFI La Silla, right: FORS1 Paranal. Credit: ESO

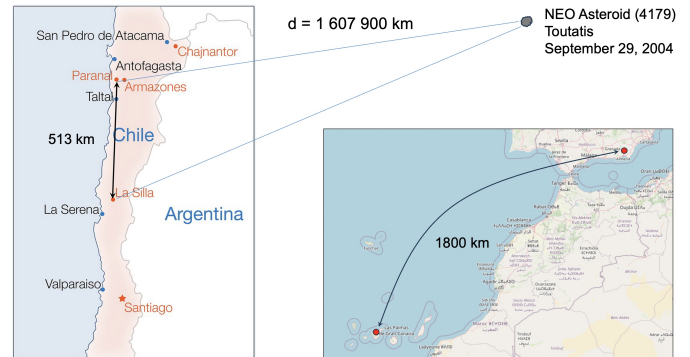


**Fig. 2.** Left: triangulation of asteroid 4179 Toutatis with 513 km baseline between ESO observatories at Paranal and La Silla. Right: 1800 km baseline of ORCA-TWIN sites on mainland Spain and Tenerife. Credit: ESO, OpenStreetMap Wiki.

two off-the-shelf innovative qCMOS cameras, along with establishing a detector lab, provided the opportunity of a quick start in the area of detector technology, image sensor characterization, and scientific application. The idea of testing the fast, low noise Hamamatsu ORCA-Quest 2 camera for high cadence synchronized observations of the same object with two telescopes at remote sites led to the definition of the ORCA-TWIN project, involving the 1.23m telescope at Calar Alto Observatory (CAHA), and one of the pair of 1.2m robotic STELLA telescopes at the Teide Observatory, Tenerife. The hypotheses that shall be tested are the expected capability to eliminate atmospheric turbulence, and the ability to directly triangulate near earth solar system objects.

The latter is illustrated by observations of the near earth passage of asteroid 4179 Toutatis that were obtained nearly simultaneously from ESO observatories Paranal and La Silla on September 29, 2004, at 02:30 hrs UTC, when the object was predicted to miss the earth by merely 1,640,000 km, i.e. four times the distance of the moon<sup>2</sup>. Figure 1 shows the tracks of the fast moving object, with an apparent magnitude of roughly 10 mag, and a velocity of  $11 \text{ km s}^{-1}$  relative to the earth, obtained from 1 min exposures through an R filter with the Wide Field Imager (WFI) at the ESO/MPG 2.2m telescope on La Silla (left), and the same through a narrowband [O III] filter with the FORS1 instrument at UT2 on Paranal (right). From the parallax of about 40 arcsec and a distance of the observatories of 513 km, the distance to the asteroid could be readily computed as 1,607,900 km (Figure 2).

We assume that under similar circumstances, but considerations of a more than three times longer baseline (Fig. 2), and

<sup>1</sup> <https://www.hamamatsu.com/us/en/product/cameras/qcmos-cameras/C15550-20UP.html>

<sup>2</sup> ESO Press Release September 29, 2004

sub-arcsec precision astrometry that will become possible with short dual ORCA-TWIN exposures, synchronized with a GPS standard to millisecond accuracy, the range of triangulation can be two to three orders of magnitudes larger than the Toutatis example, i.e. well above several A.U.

With similar arguments, low earth orbit objects (LEO), satellites, also space debris, would become accessible to fast cadence ORCA-TWIN observations as opposed to streak detection (Tonry 2011; Nir et al. 2018; Wang et al. 2022).

A science case that would explore a variant of wide field speckle imaging of stellar fields as put forward by [Bialek et al. \(2024\)](#) can potentially make use of the two different optical lines-of-sight for the ORCA-TWIN telescopes that will probe completely different turbulence profiles, making use of Information Field Theory ([Enßlin 2025](#)).

Further science cases for ORCA-TWIN include, but are not limited to:

- Photometry of very fast rotating Near Earth Objects (Beniyama et al. 2022; Pravec & Harris 2007)
- Measuring Sub-Milliarcsecond Stellar Angular Sizes from Diffraction Patterns during Asteroid Occultations (Mozurkewich et al. 2003; Hanbury Brown et al. 1974; von Braun et al. 2014; Stevens et al. 2017; Kretlow et al. 2024)
- Detecting rings around Trans-Neptunian objects and measuring sizes through observations of stellar occultations at high cadence (Ortiz et al. 2017; Morgado et al. 2023)
- M star flares and their effect on exoplanet searches (Tovar Mendoza et al. 2022; Plavchan et al. 2020)
- Pulsations and binarity of hot subdwarfs (Geier et al. 2015, 2022; Uzundag et al. 2024; Dawson et al. 2024)
- The orbital decay of LISA gravitational wave sources and SN Ia progenitors (Kupfer et al. 2015, 2020b,a, 2022)
- High cadence photometry of accreting compact white-dwarf binaries (Schwope et al. 2015; Leichty et al. 2024)
- Search for hypothetical primordial Black Holes in the solar system (Tran et al. 2024; Cuadra-Grzybowski et al. 2024; Thoss & Burkert 2025)
- Fast-cadence high-contrast Bayesian imaging with photon counting camera (Enßlin 2019; Bialek et al. 2024; Pedichini et al. 2024; Enßlin 2025)
- Identification of electromagnetic counterparts of gravitational wave mergers in concert with ULTRASAT (Dorsman et al. 2023) and the detection of kilonova false positives (Nisanke et al. 2013)

Given the swift interest from the community, the ORCA-TWIN project was formally granted as a DZA pilot project in March 2025. In collaboration with Calar Alto Observatory and the STELLA Telescopes on Teide Observatory, operated by Leibniz Institute for Astrophysics Potsdam, it was decided to implement the project on a fast track. A report on commissioning at Calar Alto in June 2025 is presented in Section 5. The installation of the second camera at STELLA is planned for early 2026.

### 3. qCMOS Image Sensor Technology

On October 17, 2024, two Hamamatsu ORCA-Quest 2 model C15550-22UP cameras were delivered to DZA, with setup and initial testing beginning in the newly established DZA Detector Lab in Görlitz. This new model distinguishes itself from the first generation ORCA-Quest as described by [Lucas et al. \(2024\)](#) and [Strakhov et al. \(2024\)](#) in that the quantum efficiency (QE) in the UV was significantly improved through an optimized AR coating on the camera window, and a factor 5 improvement of frame

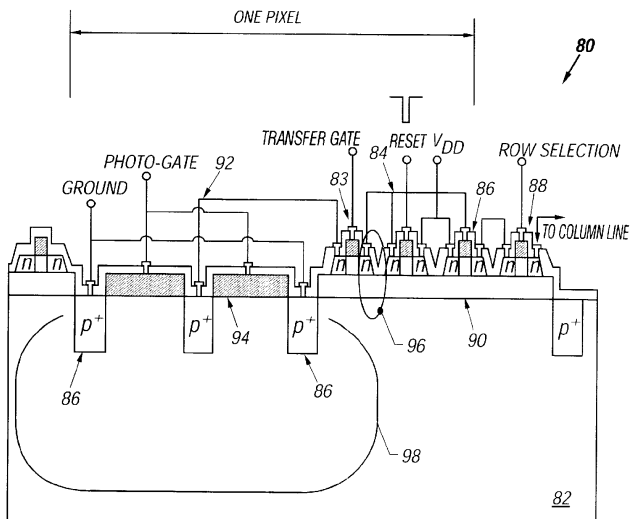


**Fig. 3.** CMOS pixel layout, including the floating transfer gate detail. Legend: pixel (80), thick low-doped p-type silicon substrate (82), transistors (83), (84), (86), (88), buried oxide insulator layer (90), photodetector area (82), polysilicon gates defining photodetector (94), deep depletion region for photo electron collection (98), reset transistor (84), buffer transistor (86), row selection transistor (88), transfer gate transistor (83), floating sense node (96). Reproduced from US Patent No. US 6,380,572 B1.

rate (25 fps) for the low readout noise mode. It has been demonstrated that the low readout noise of 0.3 e<sup>-</sup> enables detection of single photons, thus literally resolving the discrete Poissonian distribution of photon detections in the very low light level regime.

This achievement has been made possible by the optimization of the CMOS sensor chip architecture featuring an individual output node transistor for each pixel, and a multiplexer that connects the charge-to-voltage converted pixel signals to the outside circuitry.

As an example, a schematic picture of a CMOS sensor pixel architecture is shown in Figure 3. A relevant technical detail of this layout is the *floating diffusion node* (FDN), item (96) in Figure 3. It is a small, electrically isolated region of silicon that plays an important role for the conversion of photocharge to a measurable voltage. As dictated by the geometry of the node, it has a certain capacitance  $C$  that gives rise to a voltage  $U$  when it is loaded with a photocharge  $Q$  according to the elementary equation  $U = \frac{Q}{C}$ . Because the tiny geometry of the FDN and its separation from the photo-collection area (98), the capacitance is very small, hence the voltage per photocharge (conversion gain) is high. This voltage controls the output current of the amplifier, allowing the small, sensitive voltage signal to be buffered and amplified before being read out from the pixel. The FDN is "floating" because it is not connected to a fixed or controlled voltage source during the charge integration and sensing period. The reset transistor periodically discharges (resets) it to a reference voltage before a new charge integration period begins which allows to implement the correlated double sampling (CDS) noise reduction technique (Janesick 2001). Unlike the earlier realization of CDS for CCDs which happened in an external video card of the controller electronics, CMOS CDS is implemented on-chip, thus avoiding external wiring and the associated noise sources.

It is the optimization of conversion gain and CDS that enables the Hamamatsu qCMOS sensor to deliver the extremely

low readout noise figure of  $0.3 \text{ e}^-$ . As pointed out by the manufacturer, read noise depends on the square root of the bandwidth. Therefore, each column of the CMOS image sensor is supplied with its own low-pass filter circuit, so that the time needed to read out a complete line can be employed for low-pass filtering of the pixel signal selected by the pixel switch, thus reducing the readout noise even further.

A detailed study and characterization of the first generation ORCA-Quest camera was presented by [Lucas et al. \(2024\)](#). It includes a performance comparison between the ORCA-Quest upgrade and the EMCCD camera previously used in the VAMPIRES instrument within SCExAO on the Subaru telescope. The authors conclude that the qCMOS detector performs better than the EMCCD over a broad range of illuminations, especially at low-light levels.

[Krynski et al. \(2025a\)](#) have characterized the ORCA-Quest 2 camera C15550-22UP for space application, also comparing to the EMCCD. They find that for the same illumination level the qCMOS sensor has an advantage over EMCCD in terms of signal-to-noise ratio (SNR) due to high conversion gain as opposed to the multiplication mechanism of the EMCCD, where the amplification of noise explains the limiting factor at low fluxes. The low dynamic range of EMCCDs is prompting another advantage of the qCMOS sensor.

#### 4. Numerical Simulations

In order to understand in how far, despite the small pixel size, the ORCA-Quest 2 camera is competitive with regard to high performance CCD cameras, we have conducted a performance comparison between two types of commercially available sensors. The following systems that are available on the market were taken as reference and used with parameters listed in their respective data sheets: the Hamamatsu ORCA-Quest 2 camera using the  $4096 \times 2304 / 4.6 \mu\text{m}$  pixel qCMOS sensor, and the Andor iKon-L using the  $2048 \times 2048 / 13.5 \mu\text{m}$  pixel Teledyne e2v CCD. For the reasons explained in Section 3, we have passed on to include EMCCDs in the simulations as well.

The parameters used for the two camera types were taken from the manufacturer's ORCA-Quest 2 C15550-22UP datasheet<sup>3</sup>, ORCA-Quest 2 White Paper<sup>4</sup>, iKon-L 936 CCD datasheet<sup>5</sup> and are listed in the Appendix.

The simulation generates images of a star in a window of approximately  $10 \times 10 \text{ arcsec}^2$  width at the pixel sampling given by the qCMOS and CCD sensors, respectively, at the plate scale of  $20.9 \text{ arcsec mm}^{-1}$  for a telescope of  $1.23 \text{ m}$  aperture, focal length of  $9.8 \text{ m}$ , and  $0.58 \text{ m}$  diameter central obstruction. The photon flux for a star of given magnitude in a particular filter is computed from tabulated values for filters U, B, V, R, I, u, g, r, z, and multiplied with correction factors for the light collecting area of the telescope, for atmospheric extinction and quantum efficiency at the respective wavelengths, see Table A.1 in the Appendix.

The point-spread function is modeled with a Gaussian, scaled to the total stellar flux in units of photon counts for a given exposure time, the FWHM of atmospheric seeing, and then sam-

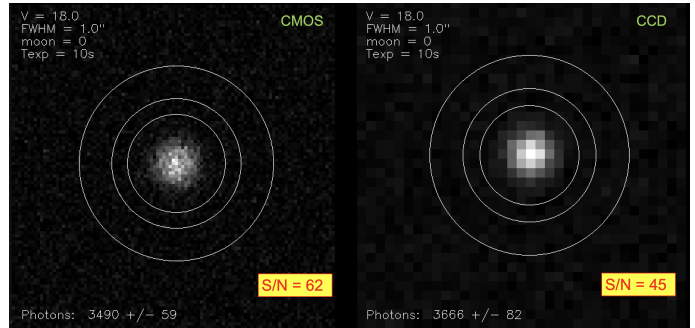


**Fig. 4.** Simulated images of a star for qCMOS (left) and CCD sensor (right), respectively, within a window of approx.  $10 \times 10 \text{ arcsec}^2$  width. The concentric circles indicate the aperture and the sky annulus for DAOPHOT photometry that is applied to the images to measure photon flux and its uncertainty.

pled at the plate scale mentioned above. Likewise, the sky background is estimated from tabulated sky surface brightness values at the wavelength of a given filter for moon phases between new and full moon (see Appendix). The uncertainty of resulting photon counts in each pixel is modeled with Poissonian noise for photoelectron counts from the star, sky, and dark current, while readout noise (RON) is applied through a Gaussian random distribution with an rms of the respective camera. RON is quoted as  $0.3 \text{ e}^-$  with readout time (ROT) 0.039 s for the ORCA-Quest 2, and  $11.7 \text{ e}^-$  with 1.65 s ROT for the iKon-L at 3 MHz unbinned operation, respectively. Modeling pixel-to-pixel response variation across the sensor was not attempted because the resulting uncertainty can be assumed to become negligible after flatfield correction ([Hu et al. 2025](#)).

Figure 4 shows an example for the simulation of a star of magnitude  $V=18.0$ , observed with an exposure time of 10 s at new moon, with a seeing of  $1.0 \text{ arcsec}$  FWHM. The different pixel sizes of the qCMOS and the CCD sensor, respectively, are immediately obvious. From images like the ones of this example, the stellar flux and its uncertainty are then measured with DAOPHOT aperture photometry, as indicated by the concentric circles in Figure 4 for the aperture and the sky annulus around the centroid of the star. The number of detected photons and its uncertainty are printed in the lower left corner of the plot.

Although at first glance the more scattered visual appearance of the qCMOS image may intuitively suggest a better result for the CCD, the measured number of detected photons and its uncertainty show the opposite: there is a factor of 1.4 SNR advantage for the qCMOS over the CCD.

The example is a good case to illustrate how very low RON wins, even in the event of extreme oversampling: if  $N$  is the number of qCMOS pixels that are equivalent to the size of a CCD pixel (in this case approximately  $N=9$ ), then the RON of the  $N$  contributing pixels adds in quadrature to  $\sqrt{N} \times \text{RON}_{\text{qCMOS}}$ , i.e.  $3 \times 0.3 \text{ e}^-$ . The resulting binned pixel noise of  $0.9 \text{ e}^-$  must be compared to the RON of  $11.7 \text{ e}^-$  at 3 MHz readout for the equivalent CCD pixel, which means a significant gain of 13.

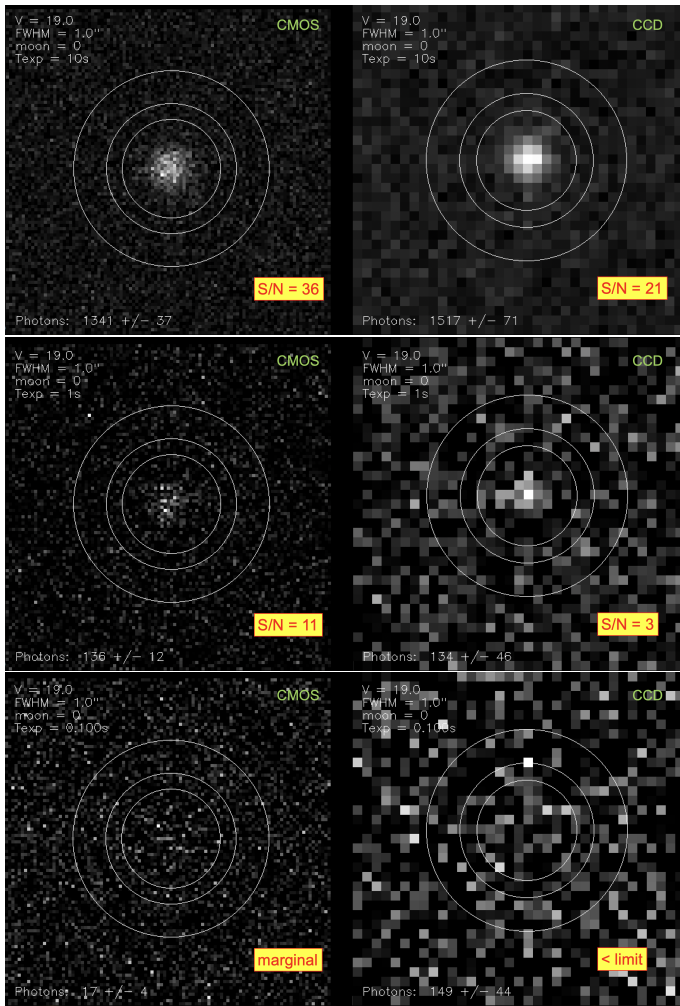
Even for the slow scan mode of 50 kHz of the CCD with  $\text{RON}=2.9 \text{ e}^-$ , there is still a gain of 3. One can go one step further and compare a  $2 \times 2$  on-chip binned CCD superpixel with 36 equivalent qCMOS pixels, resulting in  $1.8 \text{ e}^-$  versus  $11.7 \text{ e}^-$ , i.e. still a huge gain for the qCMOS.

Figure 5 illustrates this from another perspective: the same star of magnitude  $V=19.0$  observed with exposure times of 10 s, 1.0 s, and 0.1 sec, respectively. The numbers of detected photons printed in the lower left corner of the images allow to fol-

<sup>3</sup> [https://www.hamamatsu.com/content/dam/hamamatsu-photronics/sites/documents/99\\_SALES\\_LIBRARY/sys/SCAS0166E\\_C15550-22UP.pdf](https://www.hamamatsu.com/content/dam/hamamatsu-photronics/sites/documents/99_SALES_LIBRARY/sys/SCAS0166E_C15550-22UP.pdf)

<sup>4</sup> [https://www.hamamatsu.com/content/dam/hamamatsu-photronics/sites/documents/99\\_SALES\\_LIBRARY/sys/SCAS0149E\\_qCMOS\\_whitepaper.pdf](https://www.hamamatsu.com/content/dam/hamamatsu-photronics/sites/documents/99_SALES_LIBRARY/sys/SCAS0149E_qCMOS_whitepaper.pdf)

<sup>5</sup> <https://andor.oxinst.com/products/ikon-large-ccd-series/ikon-1-936>



**Fig. 5.** Simulated images in the V band for qCMOS (left) and CCD sensor (right), showing a sequence of decreasing exposure times 10 s, 1.0 s, and 0.1 s.

low the steps of a factor of 10, e.g. for the qCMOS:  $1341 \pm 37$ ,  $136 \pm 12$ ,  $17 \pm 4$  photons, which is reasonably in line with the expectation. The last image would suggest to the eye that it is pure noise, however the DAOPHOT measurement informs otherwise: a marginal SNR=4 detection. For comparison, the CCD has already reached the detection limit at this short exposure time.

Obviously, the advantage diminishes with long exposure times needed for very faint objects and background-limited observations. However, the gain for high cadence with short exposure times is clear.

It is important to emphasize the difference between shutter open time for a single exposure and the effective exposure time for a cadence of time series exposures, where the detector ROT must be subtracted from the time step between two exposures, thus clearly reducing the CCD efficiency when the time step is short enough to become comparable to the ROT.

The scatter plots for a total of 10000 simulations (Fig. 6) illustrate the situation for time series observations with a cadence between 0.1 s and 100 s for the qCMOS (top) and the CCD (bottom), respectively. The observing conditions were chosen to be photometric, new moon, and seeing 1.0 arcsec FWHM. Each blue dot represents the number of photons recovered with DAOPHOT photometry from the simulated star image with a randomly chosen cadence time step, while a corresponding red dot gives the SNR as also reported by DAOPHOT. The range

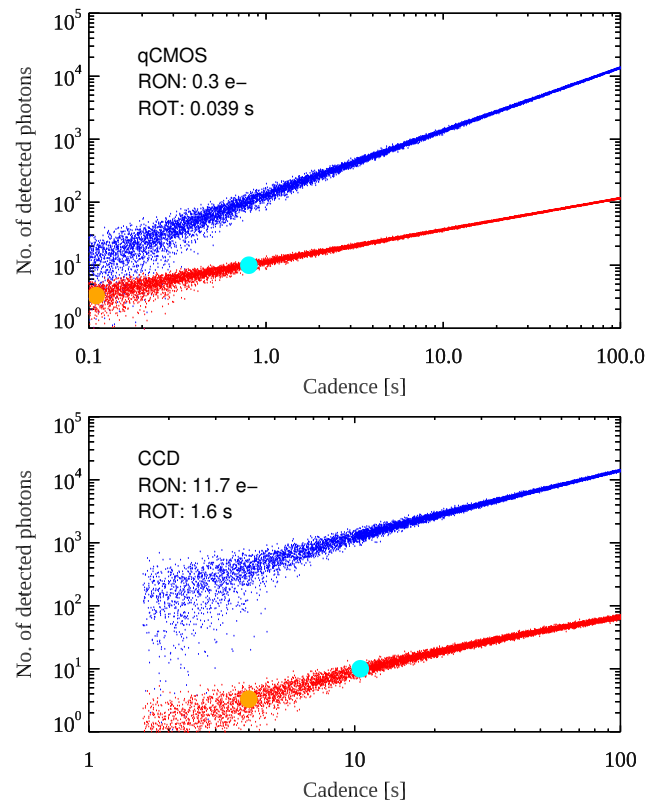


**Fig. 6.** 10.000 realisations of simulation of 19th magnitude star under excellent observing conditions, plotted as number of detected photons (blue) versus cadence time step in seconds. Red dots: Corresponding SNR distribution. The circle in orange indicates the detection limit, defined as SNR=3. The circle in cyan marks the region where exposures reach SNR=10.

of datapoints on the abscissa is truncated for the CCD at 1.6 s because a cadence shorter than the readout time does not make sense, while the range for the qCMOS extends down to a cadence of 0.1 s. Moreover, the SNR for the qCMOS is everywhere greater than the one for the CCD. The orange circles indicate the detection limit, while the circles in cyan point to the cadence where SNR=10 is reached: about 10 s for the CCD, and 0.8 s for the qCMOS. The CCD is readout noise limited in the fast readout regime, while the qCMOS is photon shot noise limited throughout.

## 5. Commissioning at Calar Alto

During a period of 4 nights allocated from June 9 to 12, 2025, the first ORCA-TWIN camera was commissioned at the 1.23m RC Telescope of Calar Alto Observatory in southern Spain. The parameters of the telescope, the resulting pixel scale, and the field-of-view are given in Table 1.

The ORCA-Quest 2 camera was mounted at the Cassegrain focus of the 1.23m telescope via a C-mount to 2 inch eyepiece adapter and additionally secured with a clamping mechanism to avoid any unwanted movement during telescope operation due to its relatively heavy mass of 3.8 kg. For data acquisition we use the Active Silicon Firebird Quad CXP-6 Frame Grabber installed in an OnLogic Karbon 803 high performance rugged control computer that was mounted at the telescope mechanical interface. The camera is operated in water-cooled mode enabling to reach minimum sensor temperatures of about  $-37^\circ$  C. As a water recirculating chiller, the Tark Thermal Solutions (formerly

**Table 1.** Telescope parameters

diameter primary mirror	1.23 m
diameter central obstruction	0.582 m
focal length	9.808 m
effective collecting area	0.922 m <sup>2</sup>
focal ratio	1/8
telescope field-of-view	90.0 arcmin
aberration-free field-of-view	15 arcmin
plate scale	20.9 arcsec/mm
projected pixel size	0.096 × 0.096 arcsec <sup>2</sup>
detector field-of-view	6.6 × 3.7 arcmin <sup>2</sup>

Laird Thermal Systems) NRC400-T0-00-PC2 is used, operating at coolant temperature of 20°C and a flow of 0.45 L/min. For GPS time synchronization the Protempis ThunderBolt GPS Disciplined Clock is employed, whose bullet antenna was placed on the outside railing of the dome.

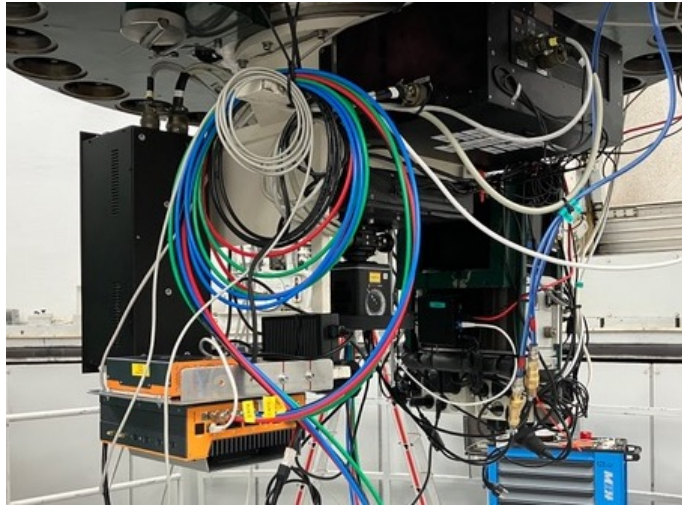


**Fig. 7.** ORCA-Quest 2 camera mounted to Cassegrain focus of CAHA 1.23m telescope. The chiller and the GPS antenna are mounted outside of the scope of the picture.

## 6. Observations

The commissioning campaign was scheduled around full moon on June 11, 2025. Weather conditions were unfavorable through the entire run, exacerbated by Calima, a dusty wind from the Sahara desert that prevented observations for most of the time. However, since the camera was swiftly made operational at daytime before the first night and the environmental conditions permitted to open the dome, First Light was obtained on June 9, 2025. Figure 8 presents a RGB color composite of the Ring Nebula M57 in Lyra, obtained between 22:51 and 23:51 UTC. Table 2 lists the exposures that have contributed to the image.

In the absence of an autoguider, the drift between exposures was compensated by registering the R and B images to the G frames. Moreover, the six brightest stars were processed with aperture photometry and registered with an equalized PSF to the G frame centroids to compensate for subtle wavelength dependent seeing differences, tracking effects, and aberrations.

In line with the scientific objective of the ORCA-TWIN project, a primary goal of the first observations was to test the capability for high cadence time resolved photometry. To



**Fig. 8.** First Light image: color composite from broad- and narrow-band filter exposures of Ring Nebula M57. Orientation: North up, East left.

**Table 2.** Details of First Light image

Filters	
R:	[S II] $\lambda\lambda$ 6717/6731 narrow band filter
G:	SDSS g broad band filter: [O III] $\lambda\lambda$ 5007/4959, H $\beta$
B:	He II $\lambda$ 4686 narrow band filter
Exposure times	
R:	5 × 180 s
G:	10 × 10 s
B:	30 × 10 s

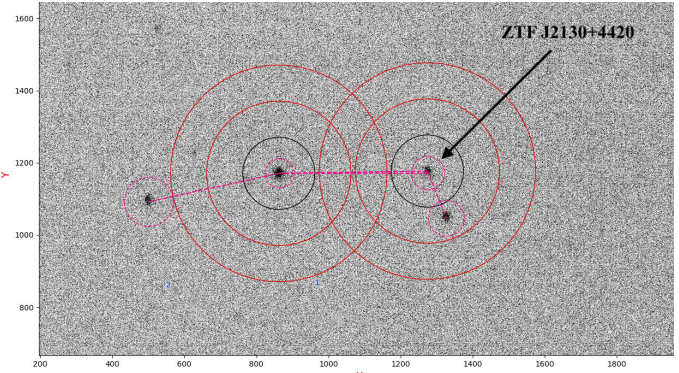


**Fig. 9.** Direct image of ZTF J2130+4420 with comparison star. The circles indicate the star apertures (black) and sky annuli (red) for aperture photometry. Orientation: North up, East left.

this end, several short period binaries were selected, out of which the ultra-compact Roche-lobe filling hot subdwarf binary ZTF J2130+4420 (Kupfer et al. 2020b) turned out to be observable on June 11, 2025, albeit under harsh conditions: full moon, scattered clouds, Calima. The object with a mean magnitude of  $g \approx 15.45$  could be observed in the Gunn g band from 01:05 UTC with a cadence of 2 s, readout time of 0.01 s at 4 × 4 pixel binning, and a total of 3047 exposures, to cover more than two periods of  $P = 39.34$  min. A preliminary data reduction was performed during the night on-the-fly by AJB using the HiPERCAM pipeline<sup>6</sup>. A direct image of the object and a comparison star for differential aperture photometry is shown in Figure 9. A fraction of the lightcurve is plotted in Figure 10. The atmospheric transmission curve illustrates the presence of clouds and very non-photometric conditions. Despite the adverse conditions, differential photometry has enabled to compensate for the variable extinction and derive a meaningful photometry. The

<sup>6</sup> <https://github.com/HiPERCAM/>

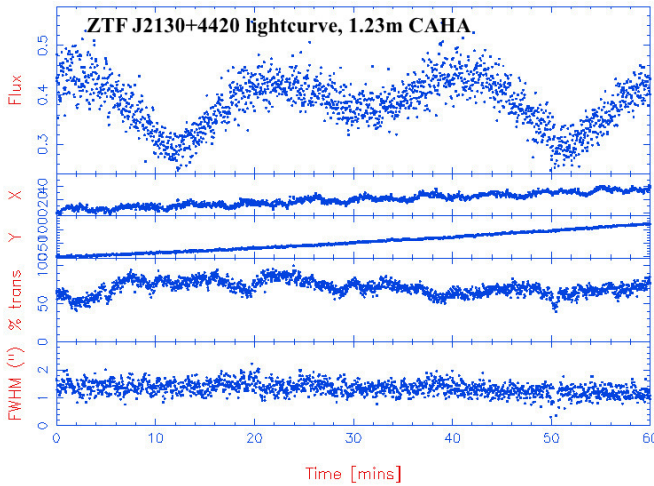


**Fig. 10.** Preliminary light curve for ZTF J2130+4420 obtained during the observing run with the HiPERCAM data reduction software (top panel). Second and third panels: telescope drift in X and Y coordinates shown in Figure 9. Fourth panel: variation of transparency of the atmosphere. Bottom: seeing FWHM in arcsec.

result compares well with the discovery light curve, Figure 1 in Kupfer et al. (2020b).

The object is interesting as a potential gravitational wave source and a possible candidate for a future SN Ia explosion. A forthcoming paper presents the full analysis of the light curve obtained in a follow-up observing run from September 2025 under good observing conditions (Teckenburg et al. 2025).

As another test case the short-period eclipsing pre-cataclysmic binary system NN Ser ( $P = 3.12$  h) could be observed partially during eclipse on June 09, 2025. NN Ser consists of a hot white dwarf ( $0.535 M_{\odot}$ ) and a main-sequence dwarf of spectral-type M4 ( $0.111 M_{\odot}$ ) with a very deep eclipse (Haefner 1989). Özdonmez et al. (2023) present modern CCD observations of the system and state that in eclipse the brightness decreases by 5.8 mag from  $V \approx 17$  mag. An analysis of the O-C diagram since 1988 reveals an orbital period variation that the authors explain with the presence of a planet of at least 9.5 Jupiter masses. ORCA-Quest 2 observations were obtained from 22:07 UTC as a series of 116 frames with 10 sec exposure time using the Gunn g filter. Unfortunately, the ingress into eclipse was missed because of a delay caused by a temporary failure of the telescope dome mechanism.

As for ZTF J2130+4420, preliminary data reduction was performed immediately during the night. The light curve shown in Figure 11 is in good agreement with Figure 1 in Özdonmez et al. (2023). Again, the non-photometric conditions can be appreciated from the variation of atmospheric transmission on the order of 50%. The case for high time resolutions is particularly important for this system as the O-C diagram analysis requires high precision, i.e. sufficiently many data points on the steep ingress and egress phases.

## 7. Conclusions

Recent years have seen increasing interest in photon counting image sensors, both in the visual, and in the near infrared, for ground based astronomy and applications in space. The commercial availability of the turnkey-ready qCMOS camera system ORCA-Quest 2 from Hamamatsu has allowed the emerging German Center for Astrophysics, that has been founded as

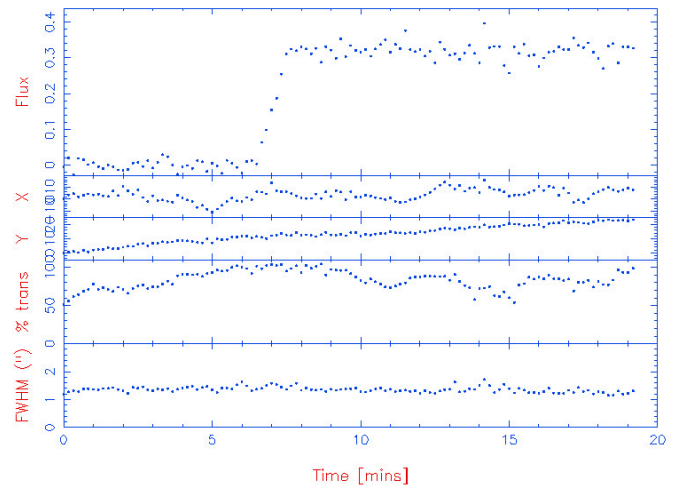


**Fig. 11.** Light curve for NN Ser. Because of a temporary technical problem related to the dome mechanism, the eclipse was only partially covered, and the ingress phase missed. For explanation see Fig. 10.

a legal entity in September 2025, to engage in this promising technology early on, and to launch the ORCA-TWIN pilot project, while creating a new center for technology, and building first collaborations with the community in Hamburg, Potsdam, Garching, and Granada (Spain). With support from Calar Alto Observatory, a fast track installation of the first ORCA-TWIN camera at the 1.23 m telescope has been accomplished at a 4 night commissioning run in June 2025, 3 months after kick-off. Despite poor, non-photometric observing conditions near full moon, First Light was obtained successfully, and the feasibility of high cadence photometry demonstrated in agreement with the predictions from numerical simulations. In the meantime, two more science observing runs were conducted in September and November 2025 whose results will be published in the near future. Forthcoming papers II. and III. will report results from characterization of the ORCA-Quest 2 in the DZA detector lab and performance during the first science observing runs, and from commissioning at the Teide Observatory, respectively.

**Acknowledgements.** Based on data obtained from the Calar Alto Observatory. MMR, PR, SV, and MK acknowledge financial support from BMFTR under grant 03WSP1745 and excellent administrative support from Projektrträger Jülich. The authors are thankful for inspiring discussions and for proposing science cases to Harry Dawson, Torsten Enßlin, Stephan Geier, Thomas Granzer, José-Luis Ortiz, Fernando Pedichini, Katja Poppenhäger, and Axel Schwöpe. We acknowledge technical support from Calar Alto Observatory and Leibniz Institute for Astrophysics Potsdam (AIP). This research was supported by Deutsche Forschungsgemeinschaft (DFG, German Research Foundation) under Germany's Excellence Strategy - EXC 2121 "Quantum Universe" – 390833306. Co-funded by the European Union (ERC, CompactBINARIES, 101078773). Views and opinions expressed are however those of the author(s) only and do not necessarily reflect those of the European Union or the European Research Council. Neither the European Union nor the granting authority can be held responsible for them.

## References

- Amico, P., Madhav, K., Hernandez, E., Roth, M. M., & Beletic, J. W. 2023, *Astronomische Nachrichten*, 344, e20230138
- Ay, S. U., Lesser, M. P., & Fossum, E. R. 2002, in *Society of Photo-Optical Instrumentation Engineers (SPIE) Conference Series*, Vol. 4836, *Survey and Other Telescope Technologies and Discoveries*, ed. J. A. Tyson & S. Wolff, 271–278
- Beniyama, J., Sako, S., Ohsawa, R., et al. 2022, *PASJ*, 74, 877
- Bessell, M. S. 1979, *PASP*, 91, 589

Bialek, S., Bertin, E., Fabbro, S., et al. 2024, MNRAS, 531, 403

Burke, B., Jorden, P., & Vu, P. 2005, Experimental Astronomy, 19, 69

Campins, H., Rieke, G. H., & Lebofsky, M. J. 1985, AJ, 90, 896

Cuadrat-Grzybowski, M., Clesse, S., Defraigne, P., Van Camp, M., & Bertrand, B. 2024, Phys. Rev. D, 110, 063029

Dawson, H., Geier, S., Heber, U., et al. 2024, A&A, 686, A25

Dorsman, B., Raaijmakers, G., Cenko, S. B., et al. 2023, ApJ, 944, 126

Enßlin, T. 2025, arXiv e-prints, arXiv:2508.17269

Enßlin, T. A. 2019, Annalen der Physik, 531, 1800127

Geier, S., Dorsch, M., Pelisoli, I., et al. 2022, A&A, 661, A113

Geier, S., Fürst, F., Ziegerer, E., et al. 2015, Science, 347, 1126

Haefner, R. 1989, A&A, 213, L15

Hanbury Brown, R., Davis, J., Lake, R. J. W., & Thompson, R. J. 1974, MNRAS, 167, 475

Hodapp, K. W. & Hall, D. N. B. 2006, in IAU Symposium, Vol. 232, The Scientific Requirements for Extremely Large Telescopes, ed. P. Whitelock, M. Dennefeld, & B. Leibundgut, 40–51

Hu, G., Mi, L., Xiao, K., et al. 2025, Scientific Reports, 15, 41088

Janesick, J., Andrews, J., Tower, J., et al. 2007, in Society of Photo-Optical Instrumentation Engineers (SPIE) Conference Series, Vol. 6690, Focal Plane Arrays for Space Telescopes III, ed. T. J. Grycewicz, C. J. Marshall, & P. G. Warren, 669003

Janesick, J., Andrews, J. T., & Elliott, T. 2006, in High Energy, Optical, and Infrared Detectors for Astronomy II, ed. D. A. Dorn & A. D. Holland, Vol. 6276, International Society for Optics and Photonics (SPIE), 62760M

Janesick, J., Gunawan, F., Dosluoglu, T., Tower, J., & McCaffrey, N. 2002, Experimental Astronomy, 14, 33

Janesick, J., Pinter, J., Potter, R., et al. 2009, in Society of Photo-Optical Instrumentation Engineers (SPIE) Conference Series, Vol. 7439, Astronomical and Space Optical Systems, ed. P. G. Warren, C. J. Marshall, R. K. Tyson, M. Lloyd-Hart, J. B. Heaney, & E. T. Kvamme, 743907

Janesick, J., Pinter, J., Potter, R., et al. 2010, in Society of Photo-Optical Instrumentation Engineers (SPIE) Conference Series, Vol. 7742, High Energy, Optical, and Infrared Detectors for Astronomy IV, ed. A. D. Holland & D. A. Dorn, 77420B

Janesick, J. R. 2001, Scientific charge-coupled devices (SPIE Press Monograph)

Jerram, P., Pool, P. J., Bell, R., et al. 2001, in Society of Photo-Optical Instrumentation Engineers (SPIE) Conference Series, Vol. 4306, Sensors and Camera Systems for Scientific, Industrial, and Digital Photography Applications II, ed. M. M. Blouke, J. Canosa, & N. Sampat, 178–186

Jerram, P. & Stefanov, K. 2020, in High Performance Silicon Imaging (Second Edition): Fundamentals and Applications of CMOS and CCD Sensors, ed. D. Durini, Woodhead Publishing, 255–287

Kretlow, M., Ortiz, J. L., Desmars, J., et al. 2024, A&A, 691, A31

Krynski, J., Bernard, V., Lalucaa, V., et al. 2025a, in Society of Photo-Optical Instrumentation Engineers (SPIE) Conference Series, Vol. 13448, Advanced Photon Counting Techniques XIX, ed. M. A. Itzler, J. C. Bienfang, & K. A. McIntosh, 134480K

Krynski, J., McGrath, D., Le Roch, A., et al. 2025b, Phys. Rev. Lett., 134, 037001

Kupfer, T., Bauer, E. B., Burdge, K. B., et al. 2020a, ApJ, 898, L25

Kupfer, T., Bauer, E. B., Marsh, T. R., et al. 2020b, ApJ, 891, 45

Kupfer, T., Bauer, E. B., van Roestel, J., et al. 2022, ApJ, 925, L12

Kupfer, T., Geier, S., Heber, U., et al. 2015, A&A, 576, A44

Leichty, M., Garnavich, P., Littlefield, C., et al. 2024, ApJ, 967, 81

Lucas, M., Norris, B., Guyon, O., et al. 2024, PASP, 136, 114504

Ma, J., Zhang, D., Elgendi, O. A., & Masoodian, S. 2021, IEEE Electron Device Letters, 42, 891

Mackay, C., Basden, A., & Bridgeland, M. 2004, in Society of Photo-Optical Instrumentation Engineers (SPIE) Conference Series, Vol. 5499, Optical and Infrared Detectors for Astronomy, ed. J. D. Garnett & J. W. Beletic, 203–209

Morgado, B. E., Sicardy, B., Braga-Ribas, F., et al. 2023, Nature, 614, 239

Mozurkewich, D., Armstrong, J. T., Hindsley, R. B., et al. 2003, AJ, 126, 2502

Nir, G., Zackay, B., & Ofek, E. O. 2018, AJ, 156, 229

Nissanke, S., Kasliwal, M., & Georgieva, A. 2013, ApJ, 767, 124

Ortiz, J. L., Santos-Sanz, P., Sicardy, B., et al. 2017, Nature, 550, 219

Özdönmez, A., Er, H., & Nasiroglu, I. 2023, MNRAS, 526, 4725

Pedichini, F., Piazzesi, R., Li Causi, G., et al. 2024, in Society of Photo-Optical Instrumentation Engineers (SPIE) Conference Series, Vol. 13097, Adaptive Optics Systems IX, ed. K. J. Jackson, D. Schmidt, & E. Vernet, 130970A

Plavchan, P., Barclay, T., Gagné, J., et al. 2020, Nature, 582, 497

Pravec, P. & Harris, A. W. 2007, Icarus, 190, 250

Roth, M. M. 2023, Astronomische Nachrichten, 344, e20230066

Schneider, D. P., Gunn, J. E., & Hoessel, J. G. 1983, ApJ, 264, 337

Schwape, A. D., Mackebrandt, F., Thinius, B. D., et al. 2015, Astronomische Nachrichten, 336, 115

Smith, N., Coates, C., Giltinan, A., et al. 2004, in Society of Photo-Optical Instrumentation Engineers (SPIE) Conference Series, Vol. 5499, Optical and Infrared Detectors for Astronomy, ed. J. D. Garnett & J. W. Beletic, 162–172

Stetson, P. B. 1987, PASP, 99, 191

Stevens, D. J., Stassun, K. G., & Gaudi, B. S. 2017, AJ, 154, 259

Strakhov, I., Safonov, B., & Cheryasov, D. 2024, in Society of Photo-Optical Instrumentation Engineers (SPIE) Conference Series, Vol. 13095, Optical and Infrared Interferometry and Imaging IX, ed. J. Kammerer, S. Sallum, & J. Sanchez-Bermudez, 130952Q

Tecklenburg, P., Kupfer, T., Brown, A. J., et al. 2025, arXiv e-prints, arXiv:2510.25653

Thoss, V. & Burkert, A. 2025, ApJ, 980, 238

Tony, J. L. 2011, PASP, 123, 58

Tovar Mendoza, G., Davenport, J. R. A., Agol, E., Jackman, J. A. G., & Hawley, S. L. 2022, AJ, 164, 17

Tran, T. X., Geller, S. R., Lehmann, B. V., & Kaiser, D. I. 2024, Phys. Rev. D, 110, 063533

Uzundag, M., Krzesinski, J., Pelisoli, I., et al. 2024, A&A, 684, A118

von Braun, K., Boyajian, T. S., van Belle, G. T., et al. 2014, MNRAS, 438, 2413

Vu, P., Fowler, B., Liu, C., et al. 2012, in Society of Photo-Optical Instrumentation Engineers (SPIE) Conference Series, Vol. 8453, High Energy, Optical, and Infrared Detectors for Astronomy V, ed. A. D. Holland & J. W. Beletic, 84530D

Wang, F., Ge, J., & Willis, K. 2022, MNRAS, 516, 5785

## Appendix A: Numerical Simulations of qCMOS versus CCD performance

The simulation of stellar images on the qCMOS and CCD cameras is coded in IDL scripts, creating images with the plate scale of a 1.23 m, f/8 focal ratio telescope, and a selectable pixel size. The resulting arrays are restricted to windows of a projected size of approximately  $10 \times 10$  arcsec $^2$ . The exact values of the parameters are listed in Table A.1 below.

On these arrays, the surface brightness distribution of a star, centered on the array, is realized with a Gaussian PSF with selectable seeing FWHM, the integral flux being normalized to 1. A more accurate Moffat profile is not deemed necessary for the simple aperture photometry used in the simulation. The physical star and sky photon counts per pixel are computed for a given magnitude in the desired broadband filter by multiplying the array with the total photon flux above the atmosphere tabulated in Table A.1, using the relation  $1 \text{ Jy} = 1.51 \cdot 10^7 \text{ photons m}^{-2} \text{ s}^{-1} \Delta\lambda/\lambda$ , multiplied with the exposure time and the throughput of the system, which is given by the quantum efficiency of the detector, atmospheric extinction, the effective light collecting area of the telescope, and reflection losses of optical surfaces. The sky background is added using the surface brightness estimates for different Moon phases as listed in Table A.1, as well as the dark current for the selected exposure time.

The resulting number of detected photons per pixel is then made subject to a Poissonian and Gaussian noise model, the former applicable to detected photons and dark current, the latter for the readout noise of the camera.

In order to create an empirical result for the detected signal and its uncertainty, aperture photometry with DAOPHOT (Stetson 1987) is applied to the final image. The aperture and inner and outer sky annulus radii are given in Table A.1.

**Table A.1.** Simulation parameters

Telescope	
diameter primary mirror	1.23 m
diameter central obstruction	0.582 m
focal length	9.808 m
plate scale	20.9 arcsec mm $^{-1}$
qCMOS	
pixel size	$4.6 \mu\text{m} \times 4.6 \mu\text{m}$
projected pixel size on the sky	$0.096 \times 0.096$ arcsec $^2$
readout noise	$0.3 \text{ e}^-$
readout time	0.039 s
dark current (-20° C)	$0.016 \text{ e}^- \text{ s}^{-1} \text{ pixel}^{-1}$
window	$103 \times 103$ pixels $^2$
	$9.96 \times 9.96$ arcsec $^2$
DAOPHOT APR	15.51 pixels
	1.5 arcsec
DAOPHOT SKYRAD	[20.67,31.01] pixels
	[2.0,3.0] arcsec
CCD	
pixel size	$13.5 \mu\text{m} \times 13.5 \mu\text{m}$
projected pixel size on the sky	$0.282 \times 0.282$ arcsec $^2$
readout noise	$11.7 \text{ e}^-$
readout time	1.6 s at 3 MHz
dark current (-80° C)	$0.00013 \text{ e}^- \text{ s}^{-1} \text{ pixel}^{-1}$
window	$35 \times 35$ pixels $^2$
	$9.94 \times 9.94$ arcsec $^2$
DAOPHOT APR	5.28 pixels
	1.5 arcsec
DAOPHOT SKYRAD	[7.04,10.57] pixels
	[2.0,3.0] arcsec

Photon Flux [photons s $^{-1}$ m $^{-2}$ above atmosphere]				
Band	$\lambda$	$\Delta\lambda/\lambda$	F(m=0) [Jy]	References
U	0.36	0.15	1810	(1)
B	0.44	0.22	4260	(1)
V	0.55	0.16	3640	(1)
R	0.64	0.23	3080	(1)
I	0.79	0.19	2550	(1)
J	1.26	0.16	1600	(2)
H	1.60	0.23	1080	(2)
K	2.22	0.23	670	(2)
g	0.52	0.14	3730	(3)
r	0.67	0.14	4490	(3)
i	0.79	0.16	4760	(3)
z	0.91	0.13	4810	(3)

Ref. (1): Bessell (1979)

Ref. (2): Campins et al. (1985)

Ref. (3): Schneider et al. (1983)

Sky brightness [mag arcsec $^{-2}$ ] with Moon phase					
Phase [d]	U	B	V	R	I
0	22.0	22.7	21.8	20.9	19.9
3	21.5	22.4	21.7	20.8	19.9
7	19.9	21.6	21.4	20.6	19.7
10	18.5	20.7	20.7	20.3	19.5
14	17.0	19.5	20.0	19.9	19.2

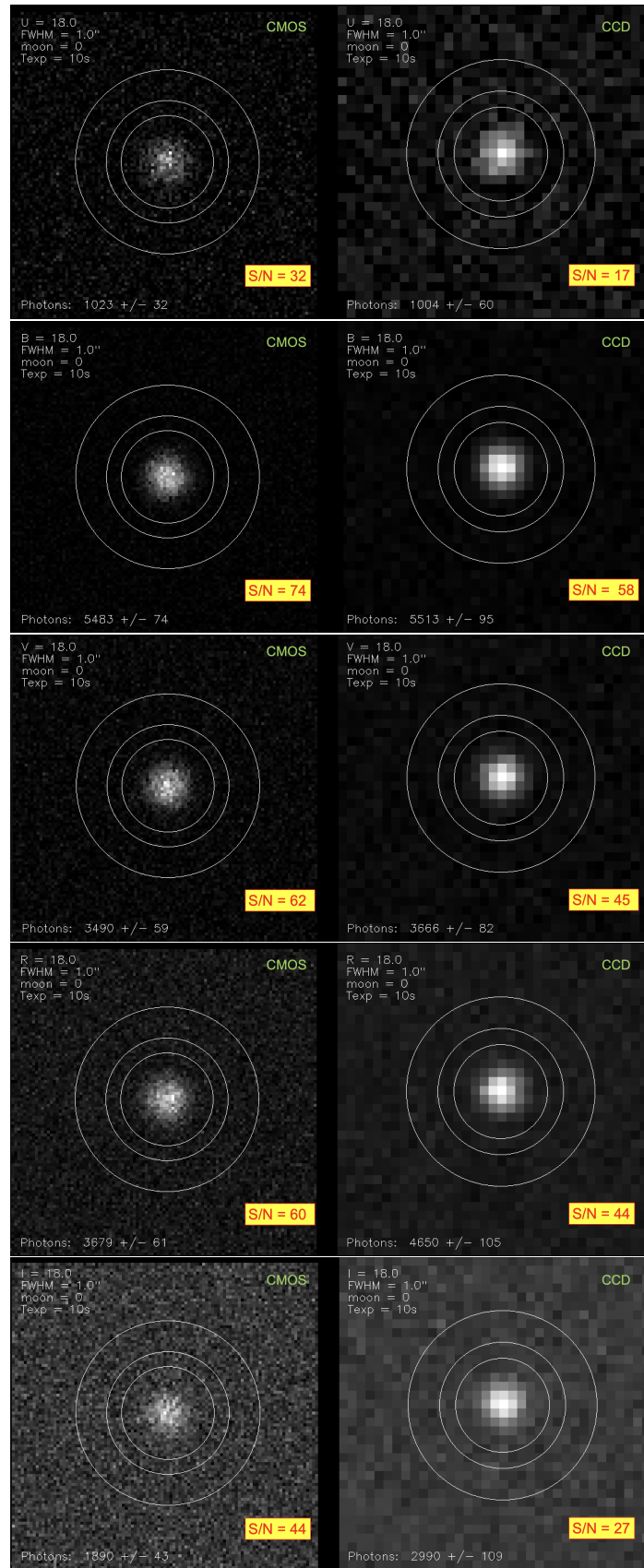


**Fig. A.1.** Simulated images for 18th magnitude star at qCMOS (left) and CCD sensor (right), for broadband filters Bessel U, B, V R, I, an exposure time of 10s, 1.0 arcsec seeing, and new moon.